Water oxidation surface mechanisms replicated by a totally inorganic tetraruthenium–oxo molecular complex

Simone Piccinin[a,1], Andrea Sartorel[b], Giuliana Aquilanti[c], Andrea Goldoni[c], Marcella Bonchio[b,1], and Stefano Fabris[a,1]

[a]Consiglio Nazionale delle Ricerche (CNR)–Istituto Officina dei Materiali (IOM) DEMOCRITOS Simulation Center and Scuola Internazionale Superiore di Studi Avanzati (SISSA), 34146 Trieste, Italy; [b]Institue of Membrane Technology of the Italian National Council of Research (ITM–CNR) and Department of Chemical Sciences, University of Padova, 35131 Padova, Italy; [c]Sincrotrone Trieste SCpA, 34149 Trieste, Italy

Edited[†] by Thomas J. Meyer, University of North Carolina, Chapel Hill, NC, and approved February 6, 2013 (received for review August 3, 2012)

Solar-to-fuel energy conversion relies on the invention of efficient catalysts enabling water oxidation through low-energy pathways. Our aerobic life is based on this strategy, mastered by the natural Photosystem II enzyme, using a tetranuclear Mn–oxo complex as oxygen evolving center. Within artificial devices, water can be oxidized efficiently on tailored metal-oxide surfaces such as RuO_2. The quest for catalyst optimization in vitro is plagued by the elusive description of the active sites on bulk oxides. Although molecular mimics of the natural catalyst have been proposed, they generally suffer from oxidative degradation under multiturnover regime. Here we investigate a nano-sized Ru_4–polyoxometalate standing as an efficient artificial catalyst featuring a totally inorganic molecular structure with enhanced stability. Experimental and computational evidence reported herein indicates that this is a unique molecular species mimicking oxygenic RuO_2 surfaces. Ru_4–polyoxometalate bridges the gap between homogeneous and heterogeneous water oxidation catalysis, leading to a breakthrough system. Density functional theory calculations show that the catalytic efficiency stems from the optimal distribution of the free energy cost to form reaction intermediates, in analogy with metal-oxide catalysts, thus providing a unifying picture for the two realms of water oxidation catalysis. These correlations among the mechanism of reaction, thermodynamic efficiency, and local structure of the active sites provide the key guidelines for the rational design of superior molecular catalysts and composite materials designed with a bottom–up approach and atomic control.

artificial photosynthesis | ab initio simulations | X-ray absorption spectroscopy | electrocatalysis

Photocatalytic water splitting offers a bioinspired strategy for replacing fossil fuels with clean energy vectors (1–3). The overall reaction entails a sequence of light-promoted electron and proton transfers coupled with cleavage and formation of molecular bonds, ultimately splitting H_2O molecules into O_2 and H_2. The application of such technology for a viable solar-fuel economy is at the forefront of a very intense research effort. The main issue is the design and optimization of innovative catalysts enabling the half reaction of water oxidation ($2H_2O \rightarrow O_2 + 4H^+ + 4e^-$) (1) at low overpotential, high turnover frequencies, and long-term operation stability. Considering its high thermodynamic cost [$E^0 = -1.23$ V at pH = 0 vs. normal hydrogen electrode (NHE)] and mechanistic complexity, water oxidation catalysis (WOC) poses severe challenges for artificial photosynthesis applications.

In plants, water oxidation is catalyzed by the Mn_4CaO_4 oxygen evolving complex of Photosystem II (PSII) enzymes. The natural catalyst exhibits a functional asset of four redox active metal centers with adjacent μ–oxo bridges to enable water oxidation with a maximal turnover frequency of 400 s^{-1} per O_2 molecule (4). The drawback lies in the intrinsic weakness of the biological components, requiring multiple repair strategies of both the inorganic core and the enzyme proteins. Similar stability issues due to oxidative damage during water oxidation affect most of the synthetic homogeneous molecular catalysts (5, 6).

In the artificial transposition of the natural process, the attention is actually focused on metal-oxide heterogeneous catalysts, which conjugate robustness and efficiency, with the most prominent examples being RuO_2, IrO_2, or cobalt phosphate (7, 8). In particular, RuO_2-based materials for electrocatalytic water oxidation have been the subject of intense investigation, including single- or polycrystalline systems (4, 9, 10), compact RuO_2 films, and composite oxides (4, 11, 12). The structure and composition of the active sites in these materials are strongly dependent on surface morphology, preparation, and doping conditions, which hinder the precise mapping of surface-absorbed species and/or detection of short-lived high-valent intermediates. As a result, the mechanism for water oxidation promoted by metal-oxide heterogeneous catalysts such as RuO_2 remains controversial. This translates into severe hurdles to fundamental studies of elementary steps and to their optimization in terms of rates and efficiency ultimately hampering the rational design of the light-absorption/conversion interface.

In this paper we identify a well-defined molecular analog to guide our understanding of the fundamental principles governing WOC at metal-oxide materials, while offering an unprecedented bridge between homogeneous and heterogeneous catalysis. Our perspective is based on the highly promising class of polyoxometalate (POM) catalysts, which comprise multinuclear metal–oxo cores embedded in totally inorganic molecular scaffolds. One of the most efficient and robust catalytic cores reported so far is a tetraruthenate oxo fragment $[Ru_4O_4(OH)_2(H_2O)_4]^{6+}$ sandwiched between two inert polyoxotungstate ligands [Ru_4–POM; Fig. 1*A*], displaying a discrete and nano-sized structure.

Ru_4–POM has been shown to oxidize water in the homogeneous phase with small overpotential (0.35 eV), high turnover frequency (>450 h^{-1}), and no degradation (13, 14). By virtue of the molecular nature, when coupled to photogenerated oxidants, it displays photo-induced electron transfer rates in the nano/microsecond time domain (15), thus approaching the natural paradigm, while preserving its activity also when it is interfaced with functionalized carbon nanotubes (16).

Our combined computational and spectroscopic study traces a parallel scenario of water oxidation at molecular Ru_4–POM and crystalline RuO_2 surfaces. We identify the thermodynamic origins and kinetic pathways governing the high efficiency of

Author contributions: S.P., A.S., M.B., and S.F. designed research; S.P. and A.S. performed research; G.A. and A.G. contributed new reagents/analytic tools; S.P., A.S., G.A., A.G., M.B., and S.F. analyzed data; and S.P., M.B., and S.F. wrote the paper.

The authors declare no conflict of interest.

[†]This Direct Submission article had a prearranged editor.

[1]To whom correspondence may be addressed. E-mail: marcella.bonchio@unipd.it, piccinin@sissa.it, or fabris@sissa.it.

This article contains supporting information online at www.pnas.org/lookup/suppl/doi:10.1073/pnas.1213486110/-/DCSupplemental.

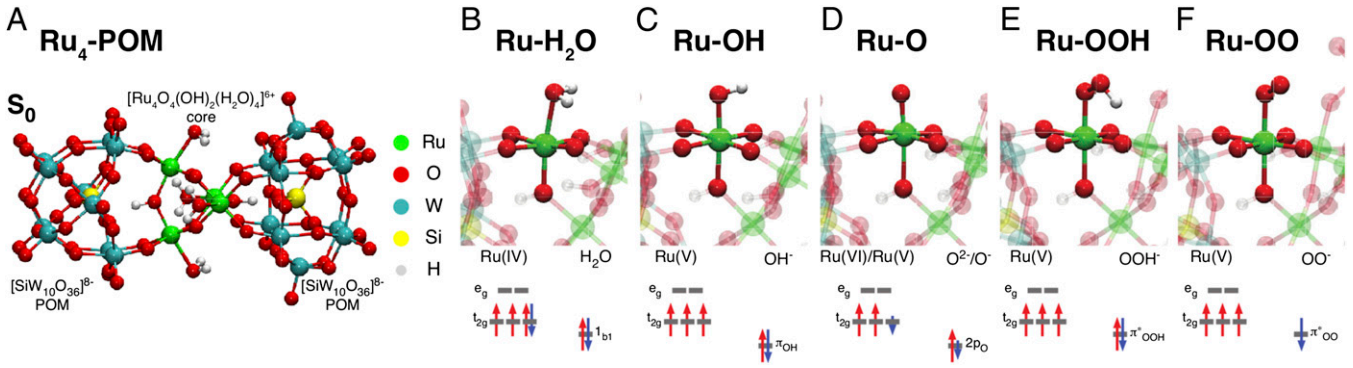

Fig. 1. (*A*) Structure of the Ru_4–POM in the resting state S_0. (*B–F*) Octahedral environment around one Ru center of Ru_4–POM, ligands involved in water oxidation and schemes of the corresponding electronic structure of the highest occupied molecular orbitals for the Ru–ligand moyeties.

the molecular Ru_4–POM and demonstrate that its elementary tetraruthenate–oxo fragment complies with the same optimal thermodynamic requirement for water oxidation displayed by crystalline RuO_2 surfaces. Disclosing the atomistic origins of the high catalytic efficiency and stability of the molecular analog opens the way for a predictive catalyst upgrade and its integration in innovative photosynthetic materials.

Results and Discussion

Ru K-Edge X-Ray Absorption Spectroscopy Analysis. We begin by demonstrating that the local atomistic and electronic structures of the metal centers in molecular Ru_4–POM and crystalline RuO_2 surfaces are equivalent. X-ray absorption near edge spectroscopy (XANES) has been performed at Ru K-edge on Ru_4–POM as isolated crystals of the cesium salt, exhibiting all Ru(IV) centers [Ru(IV)POM in Fig. 2], on a related Ru(III) complex $[Ru(H_2O)SiW_{11}O_{39}]^{5-}$, and on hydrous ruthenium oxide as prepared ($RuO_2{\cdot}xH_2O$) and after thermal activation (RuO_2 act.) at 150 °C for 5 h. The latter is a key treatment for enhancing the catalytic properties of RuO_2 crystals.

The XANES spectra (Fig. 2) have been recorded, for solid samples, on the XAFS beamline at the Elettra synchrotron source. The Ru(IV)POM and hydrous RuO_2 display identical XANES edge and line shape. The edge position is known to depend on the ruthenium oxidation state, shifting to higher photon energy as the valence state increases (17, 18). It can be concluded that the Ru ions in the two materials have the same Ru(IV) oxidation state. These data compare well with those reported for related Ru(IV) systems (18). Instead, the main absorption edge of Ru(III)POM is shifted to lower photon energies (by 2 eV), which is consistent with a lower oxidation state of Ru. It is worth noting that the pre-edge feature is practically the same for all of the samples. Moreover, the absence of adventitious Ru(III) species and or mixed valence states is evident from the position of the first absorption edge and from the line shape of the first absorption peak [note that in Ru(III)POM, the first structure is higher than the second one]. This is consistent with a silent EPR behavior of the freshly isolated crystals (19).

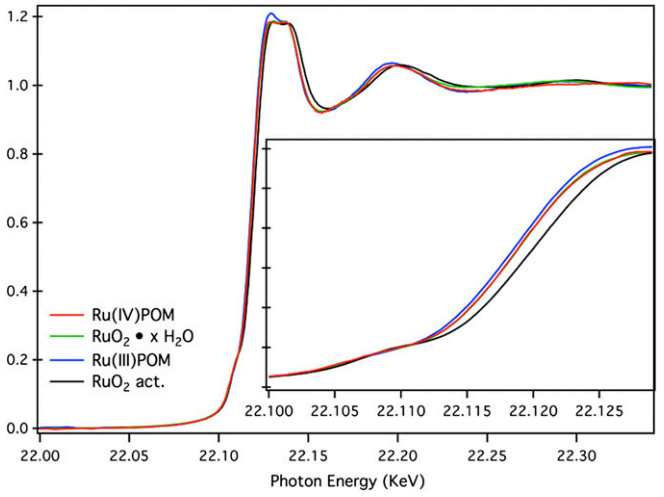

Fig. 2. XANES spectra at the Ru K edge for different Ru_4–POM [Ru(IV)POM (red) and Ru(III)POM (blue)], RuO_2 hydrous (green), and thermally activated (black). The inset shows the pre-edge and edge region of the spectra.

In addition, X-ray diffraction spectra shows that the Ru(IV) ions in both the Ru_4–POM and $RuO_2{\cdot}xH_2O$ materials have the same RuO_6 octahedral local environment with the same average Ru–O bond length, 1.98 Å (*SI Text* and Table S1). To complete the analogy, note that every Ru center of the Ru_4–POM core coordinates a water ligand and can be viewed as a minimal, highly hydrated, RuO_2 nanocrystal. Interestingly, thermally activated RuO_2 shows a shift of the peaks in the main absorption edge to higher photon energy, suggesting the evolution to less hydrated or anhydrous materials, with changed structure, in agreement with literature observation (20).

Reaction Intermediates and Thermodynamics. The equivalence in the short-range atomistic and electronic structures of the molecular and bulk ruthenium–oxide catalysts is validated by our density functional theory (DFT) calculations. These predict a distorted octahedral geometry around the Ru metal centers in the Ru_4–POM active core (21) in excellent agreement with experimental data (*SI Text* and Table S1) and similar to the one of RuO_2 crystalline surfaces. In the absence of an applied potential or without oxidants in solution, the calculations show that every Ru atom of the Ru_4–POM is in oxidation state IV and coordinates a water ligand, thus resulting in four Ru(IV)–H_2O groups (Fig. 1*A*) (13, 14, 21). In this configuration, the d^4 electrons formally residing on the metal ion in the Ru(IV)–H_2O moiety occupy the t_{2g}-like orbitals with two unpaired spins (Fig. 1*B*). This reference structure is denoted as $\mathbf{S_0}$.

From this resting state, we perform a thermochemical analysis of water oxidation adopting the computational method proposed by Norskov and coworkers (22, 23). We aim at identifying the four Ru_4–POM intermediates ($\mathbf{S_i}$, Fig. 3) that, through a cycle of four stepwise proton-coupled electron-transfer oxidations (PCET), make the formation of the O–O bond and the release of O_2 thermodynamically favorable.

The first cycle we consider begins from $\mathbf{S_0}$ and involves all of the four Ru sites of the Ru_4–POM core: $\mathbf{S_0} \rightarrow \mathbf{S_4} + 4H^+ + 4e^-$ (see cycle A in Fig. 3). The first oxidation of $\mathbf{S_0}$ leads to the

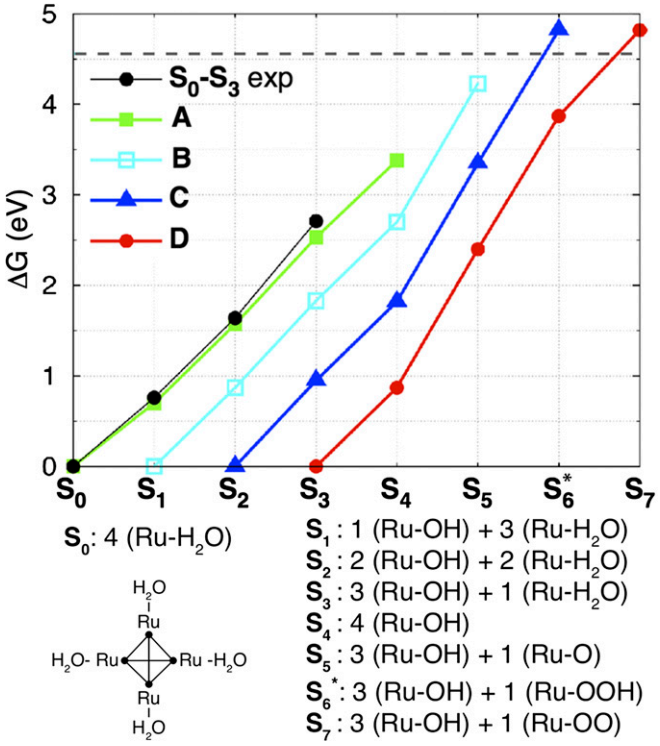

Fig. 3. (*Upper*) Calculated free energy of the four catalytic cycles for water oxidation at increasing oxidation state of Ru_4–POM. Black dots represent the available experimental values (19). Only C and D satisfy the thermodynamic requirements for water oxidation (dashed horizontal line). (*Lower*) Scheme of the tetraruthenium–oxo core in $\mathbf{S_0}$ and description of reaction intermediates $\mathbf{S_i}$.

formation of one Ru(V)–OH moiety (Fig. 1*C*) according to Ru(IV)–H_2O → Ru(V)–OH + H^+ + e^-. We denote this state as $\mathbf{S_1}$. The oxidized Ru(V) d^3 ion has three unpaired electrons in the t_{2g}-like orbitals. The successive three oxidations via PCET steps transform the other Ru(IV)–H_2O groups of $\mathbf{S_1}$ into the Ru(V)–OH ones of $\mathbf{S_2}$, $\mathbf{S_3}$, and $\mathbf{S_4}$ states (cycle A in Fig. 3).

The energetics of these four initial oxidation steps is shown in Fig. 3 (cycle A, $\mathbf{S_0} - \mathbf{S_4}$). The calculated values of the free energy differences (ΔG) are in very good agreement with the available experimental data (black circles) (Note that only the S_0–S_3 portion of the cycle is accessible experimentally) (19). This validates the high accuracy of the present computational approach [Becke 3 Lee Yang Parr (B3LYP) functional] for predicting the reaction thermodynamics. It turns out that the calculated ΔG for the $\mathbf{S_0}/\mathbf{S_4}$ couple is 3.38 eV (green line in Fig. 3), which is 1.18 eV below the thermodynamic limit for water oxidation (dashed line in Fig. 3) (While the experimental value the free energy change at standard conditions associated to the reaction $2H_2O \rightarrow O_2 + 2H_2$ is 4.92 eV, the B3LYP value, including zero point energy corrections and entropic contributions is 4.56 eV. Consistently, we will compare our B3LYP results for the energetics of the intermediates with this value rather than the experimental one.). This indicates that promoting water oxidation requires catalyst oxidation states higher than $\mathbf{S_4}$. It therefore rules out cycle A, which involves the simultaneous participation of the four Ru centers of the Ru_4–POM core.

Further oxidation of $\mathbf{S_4}$ to $\mathbf{S_5}$ leads to the formation of one formal Ru(VI)–oxo moiety (Fig. 1*D*) via the reaction Ru(V)–OH → Ru(VI)–O + H^+ + e^-. $\mathbf{S_5}$ is the highest valent intermediate in the the $\mathbf{S_1}/\mathbf{S_5}$ catalytic cycle B (Fig. 3), which entails only three Ru centers. This PCET step changes the spin density localized at the Ru atom, from 1.9 (in Ru–OH) to 1.0 (in Ru–O), and a net spin polarization appears on the oxo ligand. Note that on the basis of the charge and spin analysis, it is not possible to unambiguously associate the Ru–O moiety to a Ru(VI)–oxo or to a Ru(V)–oxyl radical (Table S2). The oxyl radical, however, has been proposed to be a key intermediate in catalytic water splitting by ruthenium complexes as in the "blue dimer" (24, 25) and also for the oxygen evolving complex of PSII (26). Similarly to cycle A, also the calculated free energy of cycle B (4.21 eV) is well below the thermodynamic limit for splitting water (Fig. 3).

The calculated thermodynamics predict that water oxidation can only be promoted by the higher valent Ru_4–POM intermediates emerging in catalytic cycles C or D (Fig. 3). These cycles require the active participation of two and one Ru centers, respectively. The computed free energy difference for both the $\mathbf{S_2}/\mathbf{S_6}$ and $\mathbf{S_3}/\mathbf{S_7}$ couples is 4.82 eV. In both these cycles, the most demanding oxidation is the formation of the first oxo moiety ($\mathbf{S_4} \rightarrow \mathbf{S_5}$, ΔG = 1.53 eV), while a lower energy cost is required to form the second Ru–oxo group ($\mathbf{S_5} \rightarrow \mathbf{S_6}$, ΔG = 1.31 eV).

In the Nørskov approach, kinetic barriers separating the intermediate states are neglected, and the overpotential is approximated by the free energy cost of the most demanding oxidation step along the cycle. In this framework, the reaction overpotential of both cycles C and D is determined by the formation of the first Ru–oxo moiety, and can be computed as $\eta = \Delta G(\mathbf{S_4} \rightarrow \mathbf{S_5}) - \Delta G(H_2O)/4 = 0.39$ eV, and is in excellent agreement with the experimental value of 0.35 eV (16). Here $\Delta G(H_2O)$ is the free energy change for the reaction $2H_2O \rightarrow O_2 + 2H_2$ at pH = 0 and room temperature.

Reaction Mechanisms for Water Splitting and O_2 Evolution. Once the catalyst has reached the activated intermediate capable of oxidizing water ($\mathbf{S_6}$), the reaction can then proceed with the key O–O bond formation step (Fig. 4). There are several possible mechanisms for this step, either intramolecular (e.g., involving an oxo ligand and an O atom of the metal-oxide core) or intermolecular (e.g., a nucleophilic attack on the Ru–oxo moiety by a solvent water molecule). The direct formation of the O–O bond from two oxo ligands in the same or in neighboring Ru_4–POM molecules can be excluded on the basis of the very large distance between the two oxo atoms in the core (> 5.26 Å) and of the reaction kinetics, respectively (13).

The lowest energy path for the O–O bond formation at one of the two Ru–oxo moieties of $\mathbf{S_6}$ was determined by metadynamics calculations (27) using as collective variable (CV) the coordination number of the oxo ligand with any other O in the system, either from the solvent or from the catalyst (Figs. S1 and S2 and other details in *SI Text*). This CV allows us to capture both the intra- and intermolecular mechanisms introduced above. This metadynamics simulation predicts that the O–O bond is preferentially formed via an intermolecular mechanism (Fig. 5*A*). It consists in the nucleophilic attack on the Ru–oxo moiety by a solvent water molecule, which evolves to a hydroperoxo ligand and liberates a proton in solution. This path is energetically more favorable than any intramolecular reaction mechanism (*SI Text*). Indeed the electronic structure of the catalyst shows the presence of low-energy empty states localized around the Ru–oxo moiety, suitable for a nucleophilic attack by water (Fig. S3).

To estimate the reaction barrier more precisely, the metadynamics simulation described above was refined by a second calculation. This time two CVs were biased: (*i*) the coordination number of one of the oxo ligands with the oxygen atom of the water molecule involved in the nucleophilic attack (CV1) and (*ii*) the coordination number of the oxygen atom of this water molecule with its two hydrogens (CV2). The free energy landscape as a function of these CVs is displayed in Fig. 5*B*. It shows that the nucleophilic attack proceeds via a concerted mechanism, in

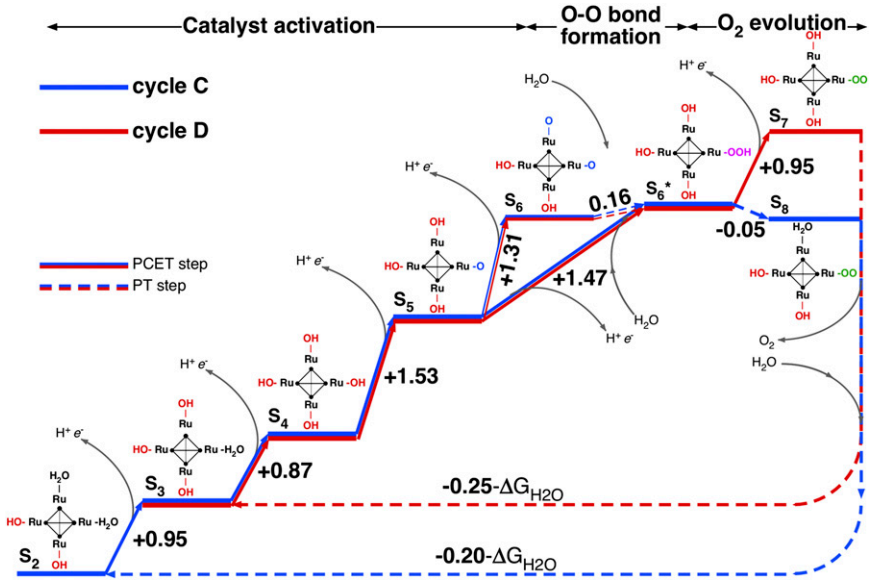

Fig. 4. Free energy diagram for cycles C and D with a schematic representation of the reaction intermediates. $\Delta G(H_2O)$ is the free energy change in the reaction $2H_2O \rightarrow O_2 + 2H_2$ at pH = 0 and room temperature.

which the formation of the O–O bond and the deprotonation of the solvent water molecule happen concurrently (Fig. S2), in analogy with what has been proposed for single-center Ru complexes (28).

Of the two Ru–oxo groups initially present in the activated $\mathbf{S_6}$ state, one converts to Ru–OOH via nucleophilic attack (as shown in our metadynamics), the other to Ru–OH by a proton transfer. In the resulting $\mathbf{S_6^*}$ intermediate (Fig. 4), all of the Ru atoms are in oxidation state V (spin density analysis in Table S2).

These simulations predict an activation energy of 0.96 eV [Perdew–Burke–Ernzerhof (PBE) functional]. Single point B3LYP calculations of two configurations representing the initial and transition states allow us to refine the free-energy barrier to 0.79 eV. By inserting this value in an Arrhenius-type equation, assuming a prefactor of 10^{13} s^{-1} and room temperature, we estimate a turnover frequency of 0.4 s^{-1}, which is in good agreement with the experimental rate, 0.12 s^{-1} at pH = 0 (13). On RuO_2, for the same non-Faradaic step leading to the formation of the OOH ligand, Fang et al. estimated the activation barrier to decrease linearly with the applied bias (29), with a slope consistent with the experimental Tafel slope. Extrapolating their results to zero bias one obtains a barrier of 0.74 eV, in the same range as our activation energy, suggesting similar kinetic requirements for the formation of the O–O bond in both systems.

By analyzing the final state predicted by these metadynamics simulations (Fig. 5*A*), we conclude that the relevant precursor of O_2 evolution is the hydroperoxo ligand of $\mathbf{S_6^*}$ (Fig. 1*E*). Its formation is slightly endothermic, $\Delta G = 0.16$ eV, as shown by the calculated thermodynamics for the $\mathbf{S_6} \rightarrow \mathbf{S_6^*}$ step (Fig. 4). Once the hydroperoxo has been formed, the reaction cycle is downhill in energy and does not involve any net transfer of electrons or protons to the electrode or solution (dashed blue line in Fig. 4). Therefore, an external potential is not required to close cycle C.

Oxygen evolution from the hydroperoxo intermediate entails two further steps. First, one of the Ru(V)–OH is converted back to a Ru(IV)–H_2O through the migration of a proton and an electron from the hydroperoxo ligand. This leads to a $O_2^{\bullet -}$ superoxo bound to the Ru(V) center ($\mathbf{S_8}$ in Figs. 4 and 1*F*). Then, an electron transfers from the superoxo to the neighboring Ru ion, and the resulting O_2 ligand is exchanged with a solvent water molecule. This leads to O_2 evolution and to the $\mathbf{S_2}$ intermediate, thus closing the catalytic cycle. Overall, the proton exchange and O_2 evolution steps are exothermic by –0.05 and –0.20 eV, respectively.

Atomistic and Thermodynamic Origins of Catalytic Efficiency: Unifying Concepts in WOC. The formation of the key hydroperoxo intermediate through the $\mathbf{S_5} \rightarrow \mathbf{S_6} \rightarrow \mathbf{S_6^*}$ sequence could also be envisioned as a single PCET step coupled to the nucleophilic attack ($\mathbf{S_5} \rightarrow \mathbf{S_6^*}$, $\Delta G = 1.47$ eV; Fig. 4). This is the same

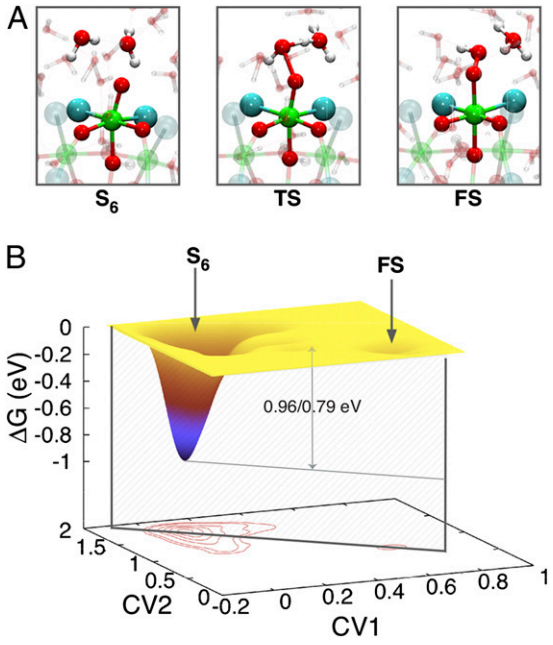

Fig. 5. Reaction mechanisms for water splitting and O–O bond formation. (*A*) Nucleophilic attack: Initial ($\mathbf{S_6}$), transition (**TS**), and final states (**FS**). (*B*) Free energy surface of the reaction as a function of the two CVs reconstructed from the metadynamics simulation. The two activation energies refer to the PBE/B3LYP functionals, respectively.

mechanism of water oxidation proposed for ideal metal and metal-oxide surfaces (30–32).

The similarity between the homogeneous and heterogeneous reaction mechanisms becomes even more evident by considering the $\mathbf{S_3 \rightarrow S_4 \rightarrow S_5 \rightarrow S_6^* \rightarrow S_7}$ path (cycle D in Fig. 3), which is energetically equivalent to the $\mathbf{S_2 \rightarrow S_6^*}$ one (cycle C) described above. Cycle D involves the same four PCET steps proposed for metal-oxide surfaces (32):

$$2H_2O \xrightarrow{\Delta G_1} OH^* + H^+ + e^- + H_2O, \quad [1]$$

$$OH^* + H^+ + e^- + H_2O \xrightarrow{\Delta G_2} O^* + 2H^+ + 2e^- + H_2O, \quad [2]$$

$$O^* + 2H^+ + 2e^- + H_2O \xrightarrow{\Delta G_3} OOH^* + 3H^+ + 3e^-, \quad [3]$$

and

$$OOH^* + 3H^+ + 3e^- \xrightarrow{\Delta G_4} O_2 + 4H^+ + 4e^-. \quad [4]$$

In both the crystalline RuO_2 and molecular Ru_4–POM cases (cycle D), the oxygen evolution cycle takes place at a single ruthenium site. It involves the hydroxo (OH*), oxo (O*), and hydroperoxo (OOH*) intermediates, which are formed electrocatalytically, and the formation of the O–O bond proceeds through the nucleophilic attack of a water molecule. This analogy sheds light on the origins of the efficiency of the Ru_4–POM complex and provides a unifying scenario governing water oxidation at molecular and crystalline metal-oxide catalysts.

In the theory of surface catalysts, maximum thermodynamic efficiency is achieved by thermodynamic stairways of metal-based intermediates that equally distribute the free energy of water oxidation (4.92 eV at pH = 0) among the four elementary steps of Eqs. **1–4**. In this way the same minimal potential (1.23 V at pH = 0, NHE) can drive all of the PCET steps, avoiding thermodynamic barriers due to uneven stability of some intermediates. For a wide class of crystalline metal and metal-oxide surfaces, the binding energies of metal-aquo/hydroxo and oxo species are shown to depend linearly one to another (32, 33). As a result, the free energy of each oxidation (ΔG_i in Eqs. **1–4**) can be expressed as linear functions of the oxygen binding energy (ΔE_O), which is taken as the reaction descriptor (32). [This linear dependence has also be shown to lead to $\Delta G_2 + \Delta G_3 = 3.2 \pm 0.2$ eV (33). Multi-site mechanisms, favored for proximal metal-group interactions and leading to intramolecular O–O coupling, would not obey the linear relationships described above and could thus brake the predicted 3.2 eV constraint.]

Fig. 6 reports the free energies for the two most demanding oxidations steps—the formation of the oxo (ΔG_2) and of the hydroperoxo (ΔG_3) intermediates—as a function of ΔE_O. The resulting volcano plot (shaded area) determines the thermodynamic overpotential (i.e., the largest ΔG_i) for a given value of the descriptor ΔE_O. The thermodynamic requirements at the top of the volcano plot (ΔE_O such that $\Delta G_2 = \Delta G_3$) set the optimal catalyst with the smallest overpotential (32). Extended screening of metal-oxide crystalline surfaces show that RuO_2(110) surfaces satisfy well these optimal thermodynamic requirements [black dot in Fig. 6; data from ref. 33 obtained using the restricted PBE (RPBE) functional for an O-covered surface]. [The black dot in Fig. 6 corresponds to the RuO_2–3O structure in (32), where O ligands are present at three out of four Ru surface sites. The oxygen adsorption energy is strongly influenced by the surface coverage: as the coverage is reduced, oxygen is more strongly bound and the corresponding point on the volcano moves to left (32).] This rationalizes why this material is among the ones displaying the smallest, albeit finite, overpotential (33).

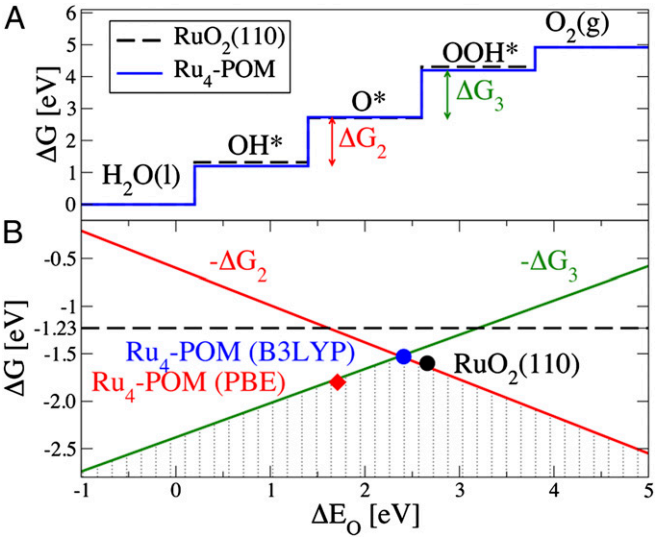

Fig. 6. (*A*) Free energies of the four PCET steps (reactions 1–4) for water oxidation on the crystalline RuO_2 surface (black line) and Ru_4–POM (blue). (*B*) Negative of free energy cost of the most demanding oxidation steps (ΔG_2 and ΔG_3) as a function of the oxygen binding energy (ΔE_O). The shaded area (volcano plot) sets the overpotential for a given value of ΔE_O.

Our calculations show that Ru_4–POM perfectly complies with the set of linear relationships established for metal oxide surfaces and is almost on top of the volcano, in close proximity with RuO_2(110) surfaces (Fig. 6). This is a clear indication that the tetraruthenate–oxo core of this molecular catalyst can be viewed as an elementary RuO_2 unit, promoting the same reaction mechanism as the parent oxide, with very similar overpotential as shown both experimentally and theoretically. In Fig. 6 we report for Ru_4–POM both data obtained with the B3LYP and PBE functionals. While for this system the use of different functionals results in significant differences in the energetics (with only hybrid functionals being able to accurately reproduce the experimental overpotential and the free energy change of the $\mathbf{S_0 \rightarrow S_3}$ transformation) (21), both data points lie on the volcano plot. This suggests that the linear relationships established using one particular functional (RPBE) (32) might be of general application.

Single- vs. Multisite Mechanisms by Molecular Cores. The thermodynamic equivalence of the two reaction pathways shown in Fig. 4 suggests that the efficiency of multicenter metal–oxo cores is not necessarily determined by multisite mechanisms involving oxidation of several metal centers of the core. Instead, the minimum overpotentials can be achieved also by reaction pathways in which a single metal site within the tetraruthenium core promotes a multielectron process, like cycle D for the Ru_4–POM. In this cycle, the nonparticipating sites remain in the Ru(V)–OH state. While metal oxidation states on the bulk material have hardly been discussed, this observation traces a parallel between cycle D and water oxidation on fully hydroxylated RuO_2 surfaces, which are predicted to be stabilized under applied bias (29, 32).

Indeed a single-site Ru–POM molecule was recently shown to catalyze the oxidation of water in the homogeneous phase (34), suggesting that cycle D could be a common mechanism at play on both single- and multicenter catalysts. Although the thermodynamic efficiency of the Ru_4–POM can be controlled by only one or two sites, the presence of multiple metal centers clearly plays an important function, as shown by the significantly superior performance of Ru_4–POM (13, 14) compared with the single center catalysts (34). The difference in their efficiency is likely

to arise from the local environment around the active sites, shaped and reinforced by the metal–oxo connectivity among them. This, together with the thermodynamic analogy between the homogeneous Ru_4–POM and the heterogeneous metal–oxo surfaces presented above, suggests that the Ru–O connectivity in the tetraruthenium–oxo core could be enough to mimic, at the active site, the structural and electronic effects of an extended RuO_2 surface.

In conclusion, we show that the efficiency of the Ru_4–POM complex, a unique tetranuclear water-oxidation catalyst, stems from thermodynamic and kinetic origins that are common to extended metal–oxide surfaces. The stepwise oxidation of the tetraruthenate core is instrumental to activate a single Ru–oxo moiety, triggering the water nucleophilic attack and O_2 release. The overpotential is minimized because the ruthenium centers can catalyze the formation of the oxo and hydroperoxo key intermediates with an almost identical cost, within the molecular tetrarutenium–oxo cores and on extended RuO_2 surfaces.

We identify a parallel scenario of water oxidation between two efficient classes of homogeneous and heterogeneous inorganic catalysts. The core of Ru_4–POM can be viewed as an optimal RuO_2 cluster in which every metal center is exposed to the solvent, thus exhibiting the highest surface area for catalysis. Although not directly involved in the chemical reaction, the metal spectators play a crucial role, providing the electronic stabilization for the building-up of a high-valent ruthenium–oxo site, capable of water oxidation. In the same environment, the hydroperoxo intermediate is also produced at low thermodynamic and kinetic cost for the overall cycle. Understanding the guidelines to enhance such interplay between the performance of the catalyst and local atomic environment around the active site will be crucial for the design of the next generation catalysts: molecules working as activated surfaces.

Materials and Methods

Simulations were based on DFT, using CP2K code (35). Our previous benchmarks (21) show that unrestricted B3LYP/aug–triple zeta valence double polarized (TZV2P) provides an accurate description of the energetics of the reactions, with errors of the order of 0.1 eV per PCET step. The thermodynamics of the catalytic cycle was studied with the Norskov protocol (22), which has already been applied to study water oxidation (30–32) and oxygen reduction (22) on metal and metal–oxide surfaces. Details on the application of this methodology to Ru_4–POM can be found in ref. 21. To reduce the computational cost of hybrid functional calculations, the energy differences among the various intermediates are evaluated on the simplified Ru_4–Cl model first (where POM ligands are substituted with Cl^- ions; ref. 21; *SI Text* and Fig. S4). The small contribution to the energy differences introduced by the presence of the POM ligands is evaluated at the PBE level (21). All calculations for the thermodynamics of the catalytic cycle are performed in vacuum, since solvent effects on the energetics of PCET reactions for this system have been shown to be negligibly small (21).

ACKNOWLEDGMENTS. We thank the Distributed European Infrastructure for Supercomputing Applications (DEISA)/Partnership for Advanced Computing in Europe (PRACE) for computational resources, A. Laio for help in the metadynamics calculations, and A. Cognigni for preliminary XANES experiments. We thank G. Scoles, M. Prato, and their teams for collaboration in the broader context of innovative nanomaterials for energy applications. This work was partially supported by the Seventh Framework Programme Marie Curie International Reintegration Grant (IRG) Program (Grant PIRG04-GA-2008-239199); by the European Cooperation in Science and Technology (COST; action number CM1104); by the Italian Ministero dell'Istruzione, dell'Universitá e della Ricerca (Firb Nanosolar RBAP11C58Y_003, PRIN HIPHUTURE 2010N3T9M4_001); and by Fondazione CARIPARO (NanoMode, progetti di Eccellenza 2010).

1. Lewis NS, Nocera DG (2006) Powering the planet: Chemical challenges in solar energy utilization. *Proc Natl Acad Sci USA* 103(43):15729–15735.
2. Balzani V, Credi A, Venturi M (2008) Photochemical conversion of solar energy. *ChemSusChem* 1(1-2):26–58.
3. Gray HB (2009) Powering the planet with solar fuel. *Nat Chem* 1(1):7.
4. Dau H, et al. (2010) The mechanism of water oxidation: From electrolysis via homogeneous to biological catalysis. *ChemCatChem* 2(7):724–761.
5. Concepcion JJ, et al. (2009) Making oxygen with ruthenium complexes. *Acc Chem Res* 42(12):1954–1965.
6. Sala X, Romero I, Rodriguez M, Escriche L, Llobet A (2009) Molecular catalysts that oxidize water to dioxygen. *Angew Chem Int Ed* 48(16):1521–3773.
7. Harriman A, Pickering IJ, Thomas JM, Christensen PA (1988) Metal oxides as heterogeneous catalysts for oxygen evolution under photochemical conditions. *J Chem Soc, Faraday Trans* 1(84):2795–2806.
8. Kanan MW, Nocera DG (2008) In situ formation of an oxygen-evolving catalyst in neutral water containing phosphate and Co^{2+}. *Science* 321(5892):1072–1075.
9. Lodi G, Sivieri E, Battisti A, Trasatti S (1978) Ruthenium dioxide-based film electrodes. *J Appl Electrochem* 8(2):135–143.
10. Castelli P, Trasatti S, Pollack FH, O'Grady WE (1986) Single-crystals as model electrocatalysts - oxygen evolution on RuO_2(110). *J Electroanal Chem* 210(1):189–194.
11. Trasatti S (2000) Electrocatalysis: Understanding the success of DSA. *Electrochim Acta* 45(15-16):2377–2385.
12. Fierro S, Nagel T, Baltruschat H, Comninellis C (2007) Investigation of the oxygen evolution reaction on Ti/IrO_2 electrodes using isotope labelling and on-line mass spectrometry. *Electrochem Commun* 9(8):1969–1974.
13. Sartorel A, et al. (2008) Polyoxometalate embedding of a tetraruthenium(IV)-oxo-core by template-directed metalation of $[\gamma\text{-}SiW_{10}O_{36}]^{8-}$: A totally inorganic oxygen-evolving catalyst. *J Am Chem Soc* 130(15):5006–5007.
14. Geletii YV, et al. (2008) An all-inorganic, stable, and highly active tetraruthenium homogeneous catalyst for water oxidation. *Angew Chem Int Ed Engl* 47(21):3896–3899.
15. Orlandi M, et al. (2010) Ruthenium polyoxometalate water splitting catalyst: Very fast hole scavenging from photogenerated oxidants. *Chem Commun (Camb)* 46(18):3152–3154.
16. Toma FM, et al. (2010) Efficient water oxidation at carbon nanotube-polyoxometalate electrocatalytic interfaces. *Nat Chem* 2(10):826–831.
17. Besson C, et al. (2011) Addition of N-heterocyclic carbenes to a ruthenium(VI) nitrido polyoxometalate: A new route to cyclic guanidines. *Inorg Chem* 50(6):2501–2506.
18. Zhan B-Z, et al. (2003) Zeolite-confined Nano-$RuO_{(2)}$: A green, selective, and efficient catalyst for aerobic alcohol oxidation. *J Am Chem Soc* 125(8):2195–2199.
19. Sartorel A, et al. (2009) Water oxidation at a tetraruthenate core stabilized by polyoxometalate ligands: Experimental and computational evidence to trace the competent intermediates. *J Am Chem Soc* 131(44):16051–16053.
20. Cormier ZR, Andreas HA, Zhang P (2011) Temperature-dependent structure and electrochemical behavior of RuO_2/carbon nanocomposites. *J Phys Chem C* 115(39):19117–19128.
21. Piccinin S, Fabris S (2011) A first principles study of water oxidation catalyzed by a tetraruthenium-oxo core embedded in polyoxometalate ligands. *Phys Chem Chem Phys* 13(17):7666–7674.
22. Norskov JK, Rossmeisl J, Logadottir A, Lindqvist L (2004) Origin of the overpotential for oxygen reduction at a fuel-cell cathode. *J Phys Chem B* 108(46):17886–17892.
23. Norskov JK, Bligaard T, Rossmeisl J, Christensen CH (2009) Towards the computational design of solid catalysts. *Nat Chem* 1(1):37–46.
24. Liu F, et al. (2008) Mechanisms of water oxidation from the blue dimer to photosystem II. *Inorg Chem* 47(6):1727–1752.
25. Yang X, Baik M-H (2006) cis,cis-[(bpy)2RuVO]2O4+ catalyzes water oxidation formally via in situ generation of radicaloid RuIV-O. *J Am Chem Soc* 128(23):7476–7485.
26. Siegbahn PEM, Crabtree RH (1999) Manganese oxyl radical intermediates and o-o bond formation in photosynthetic oxygen evolution and a proposed role for the calcium cofactor in photosystem ii. *J Am Chem Soc* 121(1):117–127.
27. Laio A, Parrinello M (2002) Escaping free-energy minima. *Proc Natl Acad Sci USA* 99(20):12562–12566.
28. Chen Z, et al. (2010) Nonaqueous catalytic water oxidation. *J Am Chem Soc* 132(50):17670–17673.
29. Fang YH, Liu ZP (2010) Mechanism and Tafel lines of electro-oxidation of water to oxygen on RuO_2(110). *J Am Chem Soc* 132(51):18214–18222.
30. Rossmeisl J, Logadottir A, Norskov JK (2005) Electrolysis of water on (oxidized) metal surfaces. *Chem Phys* 319(1–3):178–184.
31. Rossmeisl J, Nørskov JK, Taylor CD, Janik MJ, Neurock M (2006) Calculated phase diagrams for the electrochemical oxidation and reduction of water over Pt(111). *J Phys Chem B* 110(43):21833–21839.
32. Rossmeisl J, Qu Z-W, Zhu H, Kroes G-J, Norskov JK (2007) Electrolysis of water on oxide surfaces. *J Electroanal Chem* 607(1–2):83–89.
33. Man IC, et al. (2011) Universality in oxygen evolution electrocatalysis on oxide surfaces. *ChemCatChem* 3(7):1159–1165.
34. Murakami M, et al. (2011) Catalytic mechanism of water oxidation with single-site ruthenium-heteropolytungstate complexes. *J Am Chem Soc* 133(30):11605–11613.
35. VandeVondele J, et al. (2005) QUICKSTEP: Fast and accurate density functional calculations using a mixed Gaussian and plane waves approach. *Comput Phys Comm* 167(2):103–128.